

# Exceptional Field Effect and Negative Differential Conductance in Spiro-Conjugated Single-Molecule Junctions

Caiyao Yang,<sup>†</sup> Jiawen Cao,<sup>†</sup> Jin-Liang Lin,<sup>†</sup> Hao Wu, Hao-Li Zhang,<sup>\*</sup> and Xuefeng Guo<sup>\*</sup>



Cite This: *J. Am. Chem. Soc.* 2024, 146, 29703–29711



Read Online

ACCESS |



Metrics & More

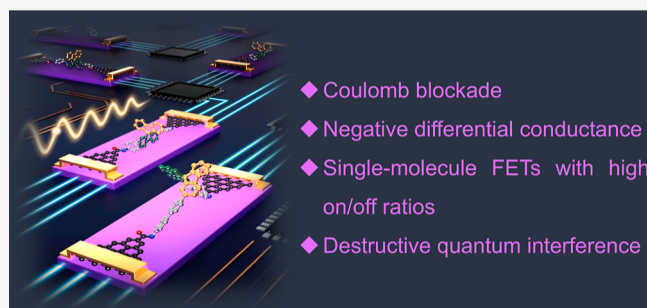


Article Recommendations



Supporting Information

**ABSTRACT:** The advancement of molecular electronics endeavors to build miniaturized electronic devices using molecules as the key building blocks by harnessing their internal structures and electronic orbitals. To date, linear planar conjugated or cross-conjugated molecules have been extensively employed in the fabrication of single-molecule devices, benefiting from their good conductivity and compatibility with electrode architectures. However, the development of multifunctional single-molecule devices, particularly those with unique charge transport properties, necessitates a more rigorous selection of molecular materials. Among different assortments of molecules suited for the construction of molecular circuits, Spiro-conjugated structures, specifically spirobifluorene derivatives, stand out as promising candidates due to their distinctive electronic properties. In this work, we focus on the charge transport characteristics of Spiro-conjugated molecules sandwiched between graphene nanogaps. Experiments reveal significant Coulomb blockade and distinct negative differential conductance effects. Beyond two-terminal device measurements, solid-state gate electrodes are utilized to create single-molecule transistors, successfully modulating the molecular energy levels to achieve an on/off ratio exceeding 1000. This endeavor not only offers valuable insights into the design and fabrication of future practical molecular devices, blessed with enhanced performance and functionality, but also presents a new paradigm for the investigation of fundamental physical phenomena.



## INTRODUCTION

Spiroconjugation, arising from the through-space orbital interaction between two  $\pi$ -systems linked orthogonally by a common tetrahedral atom, was originally proposed in 1967.<sup>1,2</sup> Molecules with the spiroconjugated structure, particularly spirobifluorene (SBF), have emerged as a key scaffold for the design of organic semiconductors in the realm of organic electronics,<sup>3</sup> finding wide applications in organic light-emitting diodes,<sup>4,5</sup> solar cells,<sup>6,7</sup> field-effect transistors (FETs),<sup>8,9</sup> etc. In the field of molecular electronics, the exploration of the SBF structures aims to leverage their rigid three-dimensional architecture to construct orientation-controlled molecular layers or molecular wires that are decoupled from the conjugated system and the metal substrate.<sup>10–12</sup>

In comparison with studies on charge transport properties of linear conjugated<sup>13,14</sup> and cross-conjugated<sup>15,16</sup> molecules, including destructive quantum interference (DQI) effects,<sup>17–19</sup> the charge transport of SBF, characterized by an orthogonal structure, may exhibit more intriguing features. For instance, it has been reported that this twisted bridge structure effectively suppresses the rate of electron transfer or tunneling.<sup>20,21</sup> Unlike linear-conjugated molecules, where  $\pi$ -electron delocalization occurs along a continuous path, the 90° twist between the conjugated units in the Spiro-conjugated structure limits the  $\pi$ -overlap, reducing the electronic coupling between the

segments. This results in localized charge transport within each conjugated unit, rather than across the entire molecule, significantly slowing the rate of charge transfer. Charge transport through the center of the SBF is considered a rate-limiting tunneling step. Moreover, the SBF fragment offers numerous substitution positions, and different functional units attached to these positions can confer distinct functionalities and topological structures on the molecules. Therefore, the charge transport properties of single-molecule junctions formed from individual SBFs, particularly the mesoscopic tunability of charge transmission, are intriguing, which is crucial for the functionalization of molecular-scale electronic devices.<sup>22–24</sup>

In this work, we designed and synthesized two SBF derivatives with distinct structural orientations: linear 2,7-SBF-NH<sub>2</sub> and orthogonal 2,2-SBF-NH<sub>2</sub>. Building upon our well-established method<sup>25–27</sup> for fabricating graphene-mole-

Received: August 9, 2024  
Revised: October 5, 2024  
Accepted: October 8, 2024  
Published: October 19, 2024



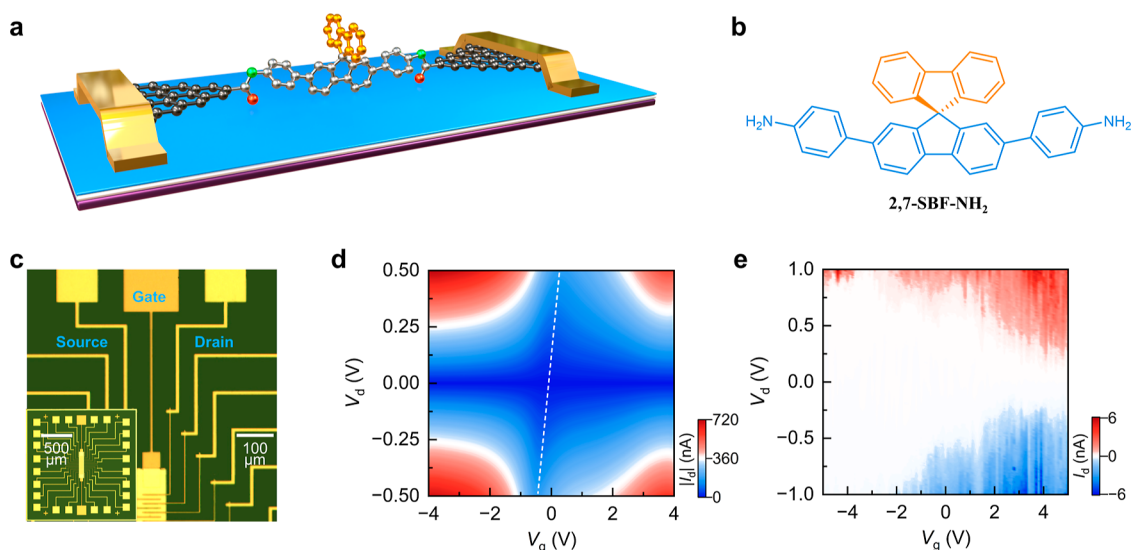


**Figure 1.** Schematic diagram of a graphene-based single-molecule FET. (a) Schematic diagram of a single-molecule device connected with 2,7-SBF-NH<sub>2</sub>. (b) Chemical structure of 2,7-SBF-NH<sub>2</sub>. (c) Optical microscopy images of a graphene FET device with Al as the bottom electrode and Al<sub>2</sub>O<sub>3</sub>/HfO<sub>2</sub> as the dielectric layer. The inset shows the complete pattern. (d) Current stability diagram for the graphene ribbon at room temperature. The dashed line shows the position of the Dirac point. (e) Current stability diagram for the device connected with 2,7-SBF-NH<sub>2</sub> at 2 K under vacuum.

cule-graphene single-molecule junctions (GMG-SMJs), we introduced a third electrode as a gate electrode to modulate the molecular energy levels. We extensively investigated the charge transport mechanism of these single-molecule junctions based on 2,7-SBF-NH<sub>2</sub>, achieving a high on/off ratio in the single-molecule FET device through gate modulation. In addition, single-molecule devices based on 2,2-SBF-NH<sub>2</sub> exhibited a negative differential conductance (NDC) effect, which was theoretically attributed to the bias-driven structural distortion that partially alleviated the DQI effect.<sup>28</sup>

## RESULTS

**Fabrication of Graphene-Based Single-Molecule Junctions.** Initially, on a pristine silicon substrate, pre-evaporated aluminum metal is employed as the gate electrode, while naturally oxidized aluminum oxide and atomic layer-deposited HfO<sub>2</sub> with a thickness of approximately 5 nm serves as the dielectric layer. Subsequently, graphene is transferred onto the surface of the dielectric layer and patterned graphene strips as well as source and drain electrodes are fabricated using photolithography and thermal evaporation, resulting in an array of graphene FETs. Lastly, dashed-line electron-beam lithography is utilized to construct nanoscale electrode gaps, and SBF derivatives are covalently anchored via amide bonds through a chemical reaction. The molecular synthesis, device fabrication procedures, and graphene FETs are presented in Figures S1–S3. Figure 1a–c shows the schematic diagram and optical microscopy images of graphene-based single-molecule devices constructed with 2,7-SBF-NH<sub>2</sub>. In order to confirm the stability and gate modulation performance of graphene FETs,  $I$ – $V$  curves (Figure 1d) at different gate voltages and transfer characteristics (Figure S4) were measured. The dashed lines in the graph demonstrate the tuning effect of the gate voltage on the graphene Dirac point, confirming stable gate modulation performance. In addition,  $I$ – $V$  measurements under different gate voltages were performed before and after the molecular connection, resulting in the current stability diagrams, i.e., three-dimensional plots of source-drain current

( $I_d$ ) as a function of gate voltage ( $V_g$ ) and source-drain voltage ( $V_d$ ), as shown in Figure S5 (empty nanogaps) and Figure 1e, respectively. In the low bias region, the single-molecule device exhibits negligible conduction, which is indicative of Coulomb blockade.<sup>29–31</sup>

**Temperature-Dependent  $I$ – $V$  Measurements and Coulomb Blockade.** Typical temperature-dependent  $I$ – $V$  curves and charge transport properties of the devices connected with 2,7-SBF-NH<sub>2</sub> are shown in Figures 2a and S6–S14. The magnitude of the current under a given bias voltage follows an exponential decrease with decreasing temperature, demonstrating a significant temperature dependence. As the temperature decreases, the  $I$ – $V$  curves near a zero bias exhibit increasingly nonlinear S-shaped characteristics. Notably, pronounced Coulomb blockade phenomena are observed within specific bias voltage ranges, and the minimum threshold voltage ( $V_T$ ) for conduction increases as the temperature decreases.

In order to study the effect of temperature on the Coulomb blockade, we analyzed  $I$ – $V$  curves obtained at different temperatures and fitted the  $V_T$  values, as well as the exponent  $\xi$  characterizing the power-law relationship between  $I_d$  and  $V_d$  when  $V_d$  exceeds  $V_T$ , using the Levenberg–Marquardt nonlinear least-squares method (Figure 2b).<sup>32,33</sup> With an increase in temperature,  $V_T$  decreases. Above 160 K,  $V_T$  falls below 5 mV, aligning with the 5 mV voltage scan step in measurements, indicating the point at which the current blockade is released. Each device exhibits a current blockade, although the  $V_T$  values vary among devices, and the current blockade can be overcome by thermal activation, surpassing the Coulomb-energy gap.

The Arrhenius plot is a prominent tool for revealing the transition of charge transport in molecular junctions from temperature-independent coherent tunneling at low temperatures to temperature-dependent incoherent hopping at high temperatures.<sup>34–36</sup> Based on the temperature-dependent  $I$ – $V$  curves, we plotted  $\ln I_d$  as a function of  $1000/T$  in Figure 2c. At low temperatures, there is no significant temperature

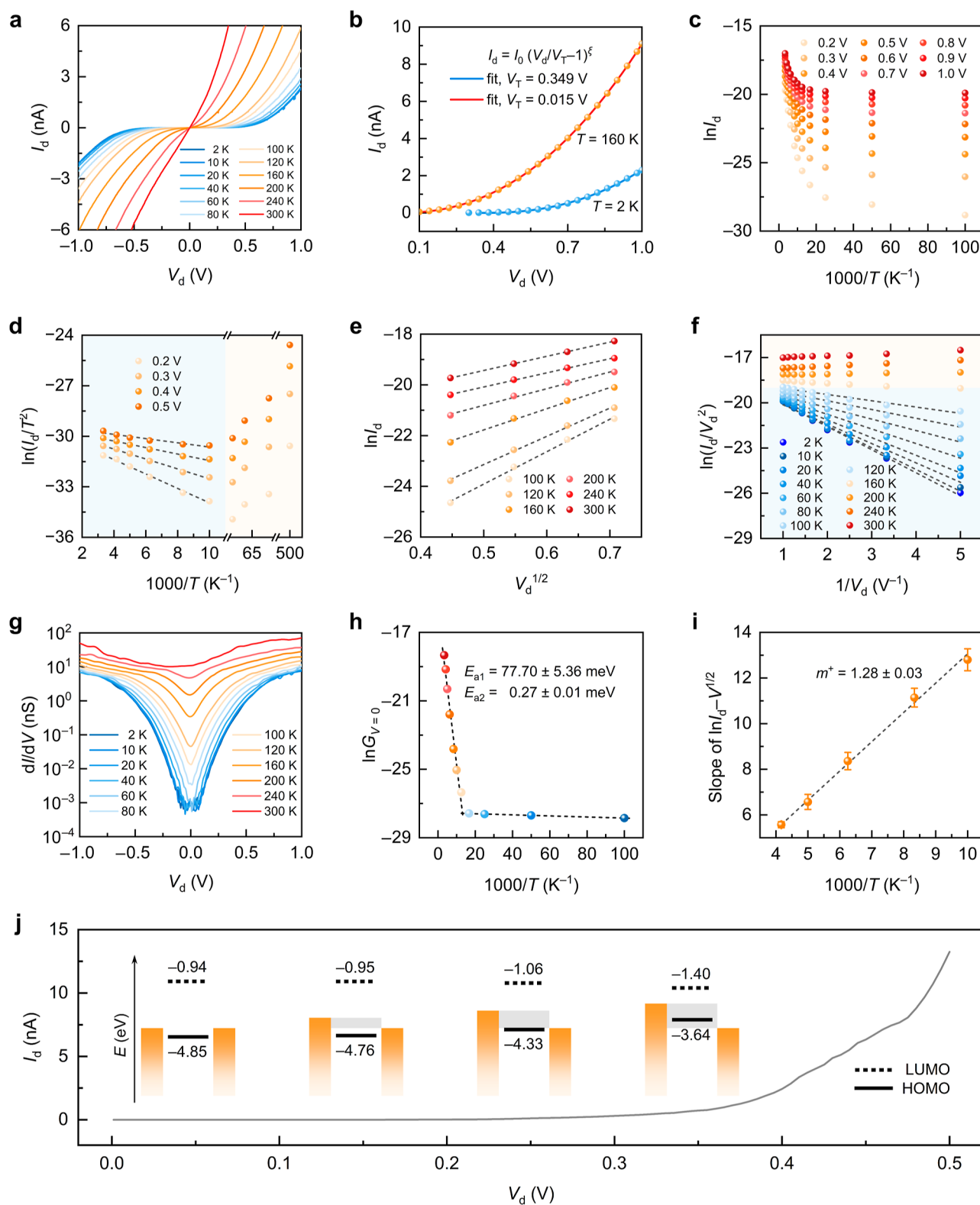


**Figure 2.** Temperature-dependent measurements and analyses of charge transport mechanism. (a)  $I$ – $V$  curves at different temperatures for a single-molecule device connected with 2,7-SBF-NH<sub>2</sub>. (b)  $I$ – $V$  curves and their fits at  $T = 2$  and 160 K at positive bias voltages, fitted by the Levenberg–Marquardt nonlinear least-squares method. (c) Arrhenius plots of  $\ln I_d$  versus  $1000/T$  at different positive bias voltages with a bias step of 0.1 V. (d) Plots of  $\ln(I_d/T^2)$  versus  $1000/T$  at different positive bias voltages. (e) Plots of  $\ln I_d$  versus  $V_d^{1/2}$  at different temperatures. (f) Plots of  $\ln(I_d/V_d^2)$  versus  $1/V_d$  at different temperatures. (g)  $dI/dV$  traces at different temperatures displayed logarithmically for a better visibility of the Coulomb blockade regime and threshold voltages. (h) Plot of  $\ln G_{V=0}$  versus  $1000/T$  for the temperature range from 10 to 200 K. (i) Plot of the slope of  $\ln I_d - V_d^{1/2}$  versus  $1000/T$  at positive bias voltages. The error bars correspond to the standard deviation of the slope fit for data points in (e). (j) Schematic of Frontier molecular orbitals alignment under varying electric field strengths. The Fermi level of graphene electrodes is  $-4.23$  eV.<sup>40</sup>

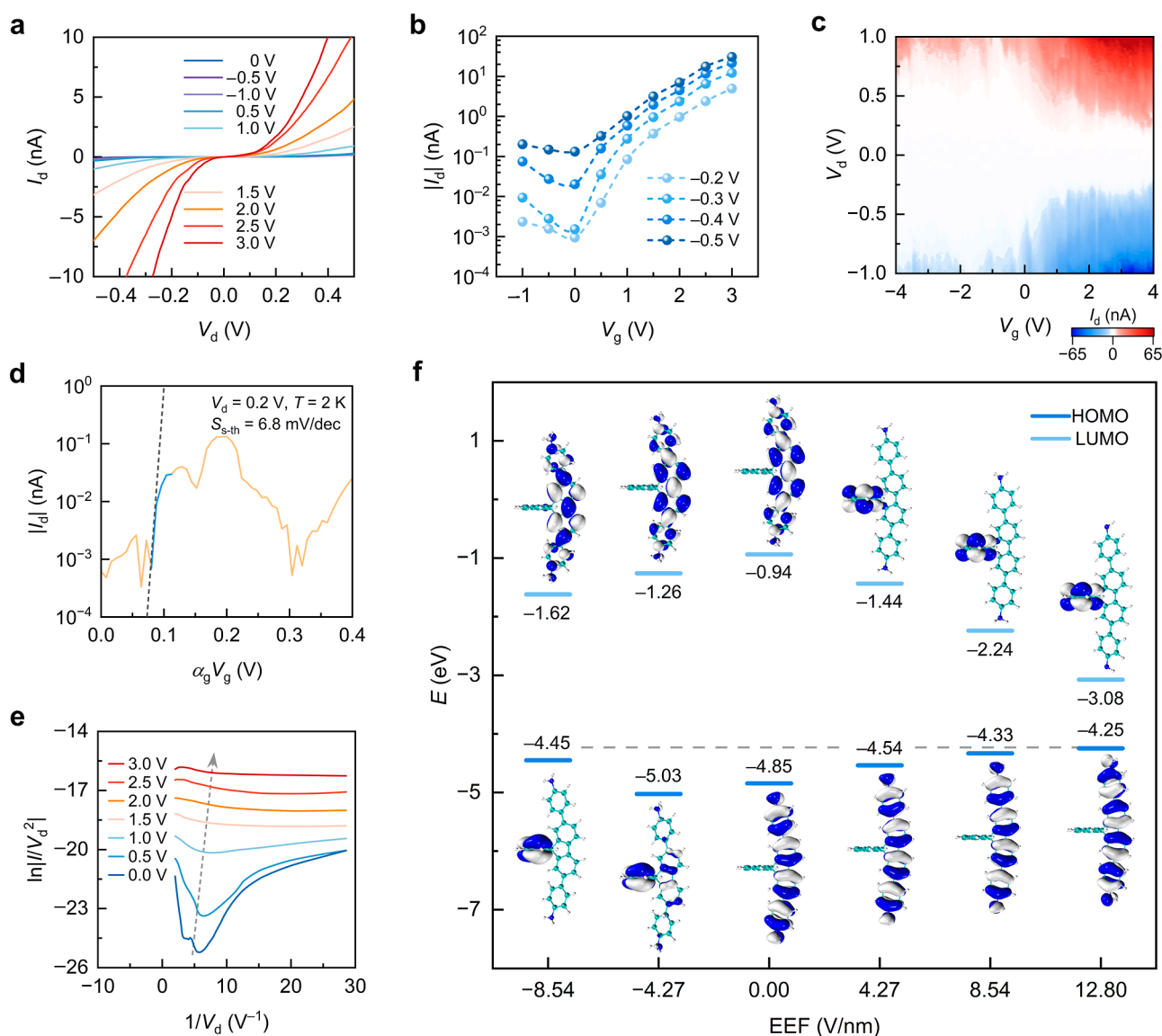


**Figure 3.** Gate-controlled charge transport characteristics of single-molecule transistors. (a)  $I$ - $V$  curves at different gate voltages ( $V_g$ ) from  $-1.0$  to  $+3.0$  V with  $\Delta V_g = 0.5$  V. (b) Transfer characteristics at different negative bias voltages. (c) Current stability diagram of the device at 2 K, showing a Coulomb blockade feature. (d) Threshold swing of the device with an estimated gate coupling parameter  $\alpha_g$  of  $\sim 0.1$ . (e) Fowler-Nordheim plots at different gate voltages under a negative bias. Dashed positions correspond to transition voltages ( $V_{\text{trans}}$ ). (f) Schematic of Frontier molecular orbitals alignment under varying EEF strengths. The dashed line represents the Fermi level of graphene electrodes, which is  $-4.23$  eV.

dependence, while in the  $T \geq 100$  K region, a clear linear correlation emerges, indicating a hopping transport mechanism. The activation energy for hopping,  $\Delta E = -(1/k_B)[d(\ln I_d)/d(1/T)]$ , decreases with increasing bias voltages (Figure S11).

In addition, we plotted  $\ln(I_d/T^2)$  versus  $1000/T$  and  $\ln I_d$  versus  $V_d^{1/2}$  in Figure 2d,e. Remarkably, both plots exhibit a clear linear correlation in a region of  $T \geq 100$  K and  $V_d \leq 0.5$  V, well described by the Richardson-Schottky (RS) equation<sup>37</sup> for thermionic emission

$$I_d = A^* T^2 \exp \left[ \frac{-(\Phi - \sqrt{q^3 V_d / 4\pi\epsilon_0 \epsilon d})}{k_B T} \right] \quad (1)$$

where  $A^*$  is the effective Richardson constant multiplied by the current injection area,  $\Phi$  is the barrier height,  $q$  is the electron charge,  $\epsilon_0$  is the vacuum dielectric constant,  $\epsilon$  is the relative

dielectric constant of the molecule,  $d$  is the length of the molecule, and  $k_B$  is the Boltzmann constant. Linear fitting analyses in Figure S12c,d determined  $\Phi$  to be  $81.7 \pm 3.7$  and  $85.1 \pm 2.8$  meV for positive and negative bias voltages, respectively.

For the region of  $T \leq 120$  K, plots of  $\ln(I_d/V_d^2)$  versus  $1/V_d$  (Figure 2f) displays a clear negative linear correlation, indicating that Fowler-Nordheim (F-N) tunneling dominates charge transport in the low-temperature high-bias region.<sup>38</sup> Consequently,  $T = 100$  K marks a distinct boundary between F-N tunneling and thermionic emission mechanisms. The significant decrease in  $V_T$  values above 100 K aligns with the transition of the transport mechanism.

The differential conductance ( $dI/dV$ ) of the device at different temperatures (Figure 2g) indicates an increasing width of the Coulomb blockade region with decreasing the temperature. In addition, the zero-bias conductance ( $G_{V=0}$ ) exhibits exponential growth with the temperature. By employ-

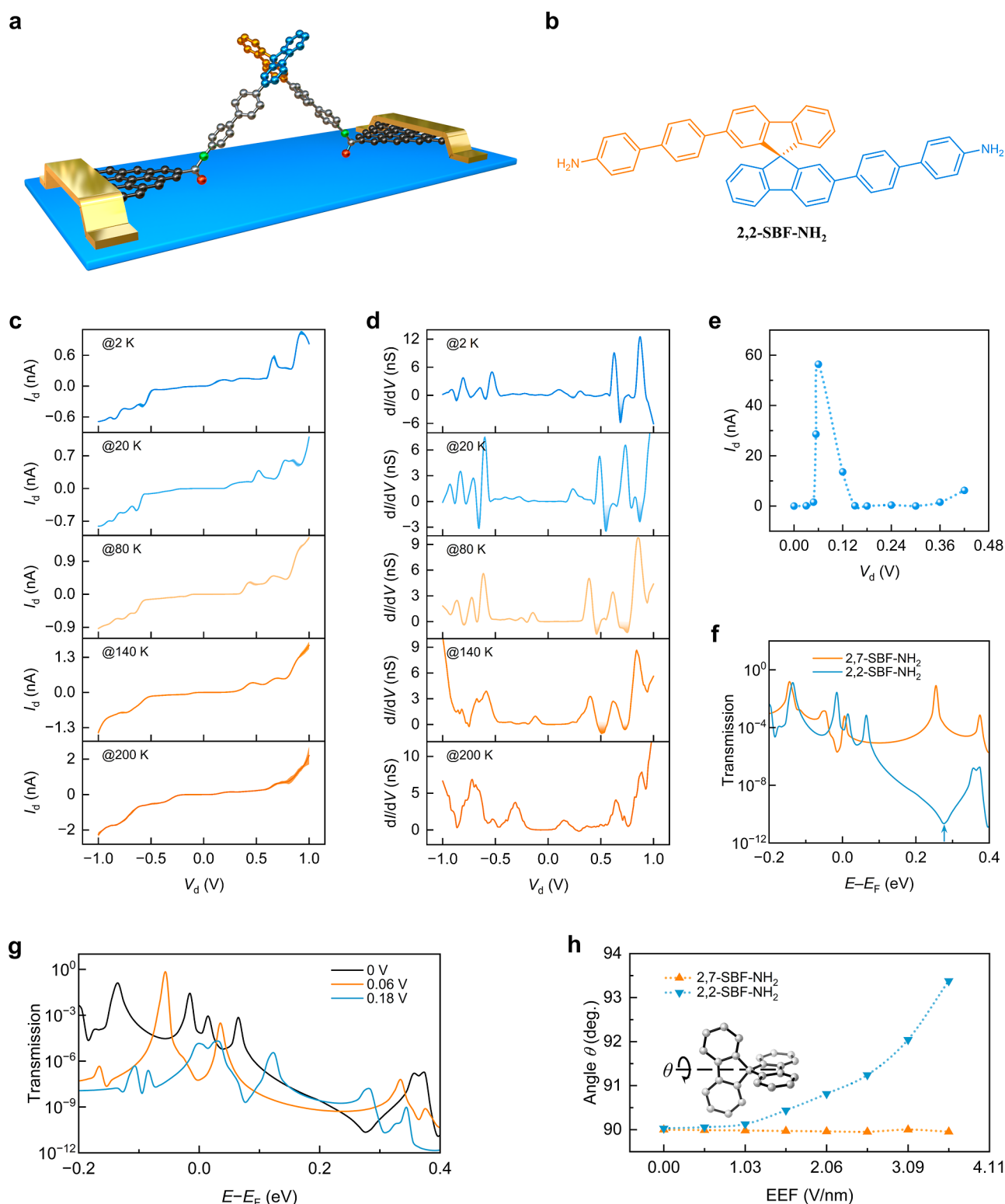


**Figure 4.** NDC effect of a device connected with 2,2-SBF-NH<sub>2</sub>. (a) Schematic diagram of a single-molecule device connected with 2,2-SBF-NH<sub>2</sub>. (b) Chemical structure of 2,2-SBF-NH<sub>2</sub>. (c)  $I$ - $V$  curves at  $T = 20, 80,$  and  $200$  K. Each curve is the average of 5 measurements. (d)  $dI/dV$  traces at different temperatures from (c), region where  $dI/dV < 0$  are colored and filled to highlight the NDC effect. (e) Theoretically calculated  $I$ - $V$  curves. (f) Transmission spectra of 2,7-SBF-NH<sub>2</sub> and 2,2-SBF-NH<sub>2</sub> at the zero bias voltage. (g) Transmission spectra of 2,2-SBF-NH<sub>2</sub> at several bias voltages. (h) Theoretically calculated dihedral angle values of the central SBF as a function of the EEF strength.

ing a simple model of electron transport in Coulomb islands,<sup>32,33</sup> where  $G_{V=0} \propto \exp[-E_a/k_B T]$ , we generated plots of the  $G_{V=0}$  curves at different temperatures to analyze the thermal activation energy ( $E_a$ ). Notably, well-defined Arrhenius behaviors are observed in both the high-temperature ( $T \geq 100$  K) and low-temperature ( $T < 100$  K) regions, with  $E_{a1} = 77.30 \pm 5.36$  meV and  $E_{a2} = 0.27 \pm 0.01$  meV, respectively, as determined through linear fitting (Figure 2h).

Such a significant difference in  $E_a$  between low- and high-temperature regions arises from the transition from tunneling to thermionic emission mechanisms at elevated temperatures. The Coulomb charging energy can be expressed as  $U = e^2/2C_0$ ,<sup>39</sup> where the capacitance  $C_0$  depends on the product of the surrounding dielectric constant ( $\epsilon$ ) and the Coulomb island radius ( $r$ ), i.e.,  $C_0 = 4\pi\epsilon_0\epsilon r$ . Assuming that the Coulomb island radius approximates the length of the molecule,  $C_0$  could be calculated using eq 1. We further plotted the slope of  $\ln I_d - V_d^{1/2}$  as a function of  $1000/T$  (Figures 2i and S14) and obtained slopes of  $m^+ = 1.28 \pm 0.03$  and  $m^- = 1.40 \pm 0.08$  for the positive and negative bias regions, respectively. Moreover,  $C_0$  was determined to be  $\sim 13$  and  $\sim 11$  aF, with the corresponding Coulomb charging energies  $U$  of  $\sim 6.12$  and  $\sim 7.24$  meV. Evidently, at low temperatures ( $T < 100$  K), the thermal activation energy  $E_{a1}$  is significantly smaller than  $U$ , leading to Coulomb blockade. Conversely, when  $T \geq 100$  K, the thermal activation energy  $E_{a2}$  is much larger than  $U$ , lifting the current blockade.

The density functional theory calculations were conducted to determine the energy levels of the molecular Frontier orbital under varying external electric field (EEF) strengths (induced by bias voltages), and the schematic of the energy level alignments is illustrated in Figure 2j. Within a certain bias range, although the energy gap ( $\Delta E_{\text{gap}}$ ) between the highest occupied molecular orbital (HOMO) and the lowest unoccupied molecular orbital (LUMO) decreases as the bias increases, and the HOMO gradually approaches the Fermi level of graphene electrodes. However, the Frontier orbitals remain outside the Fermi window, keeping the device in a current blockade state. When the bias exceeds a critical value, the HOMO level enters the Fermi window, and the  $\Delta E_{\text{gap}}$  further reduces, leading to a rapid current increase. At higher temperatures, the energy distribution of electrons in source and drain electrodes broadens (the Fermi–Dirac distribution widens), allowing the molecular HOMO level to enter the Fermi window earlier, leading to a reduced Coulomb blockade region.

**Gate-Controllable Charge Transport.** By employing thermal activation or increasing the bias voltage, it is possible to effectively decrease the Coulomb energy barrier and eliminate the Coulomb blockade. However, the Coulomb blockade effect can be harnessed as a strategic approach to construct FETs with a high on/off ratio owing to their lower off-state currents. As depicted in Figure 3a, the device shows negligible modulation of the  $I$ – $V$  curves under negative gate voltages, while significant modulation is observed under positive gate voltages, resulting in a noteworthy increase in current as the gate voltage increases. The current values corresponding to different gate voltages were extracted within a bias voltage range of  $-0.2$  to  $-0.5$  V, and the transfer characteristics are plotted, as illustrated in Figures 3b and S15. The device demonstrates a maximum on/off ratio exceeding 1000, with a negligible gate leakage current. Coulomb blockade effects were also observed in the current stability diagrams of other devices (Figures 3c and S16–S19). Under negative gate voltages, the blockade region remained almost unchanged, while, under positive gate voltages, the width of the blockade region decreased with increasing gate voltage. In particular, at lower temperatures and bias voltages, these devices exhibited an on/off ratio exceeding 1000, primarily due to Coulomb blockade in the low-temperature and low-bias regions, resulting in an extremely small off-state current.

Moreover, the temperature-dependent current stability diagram (Figure S19) showed a trend of decreasing the Coulomb blockade width with an increase in temperature, which is consistent with the temperature-dependent experimental results described earlier. Based on the current stability diagrams, we estimated the gate coupling parameter ( $\alpha_g$ ) for different devices and calculated the corresponding subthreshold swing ( $S_{s\text{-th}}$ ), as presented in Figures 3d and S20–S21. At a temperature of 2 K and a bias of 0.2 V, the lowest  $S_{s\text{-th}}$  achieved was  $\sim 6.8$  mV/dec. While variations in the interface between the molecule and graphene electrodes, as well as the dielectric layer, can lead to the difference in FET properties among devices, the strategy of utilizing a Coulomb blockade to construct FET devices with a high on/off ratio has been convincingly proven effective.

To elucidate the modulation of molecular energy levels by gate voltages, F–N plots<sup>41</sup> were generated at different gate voltages, as shown in Figures 3e and S22. The position of the dashed line in the figure corresponds to the transition voltage ( $V_{\text{trans}}$ ), which marks the boundary between F–N tunneling and direct tunneling mechanisms and exhibits a pronounced dependency on positive gate voltages. When a higher gate voltage is applied,  $V_{\text{trans}}$  shifts to a lower bias voltage. These findings demonstrate that gate voltage, especially the positive gate voltage, can effectively regulate the energy levels of molecular orbitals.<sup>41,42</sup> Figure 3f presents the calculated energy levels of HOMO/LUMO under varying EEF strengths (induced by gate voltages), where the HOMO energy level, being closer to the Fermi level of graphene, primarily contributes to charge transport. As the gate voltage increases, the energy gap  $\Delta E_{\text{gap}}$  between the HOMO and LUMO decreases, with a more pronounced reduction under a positive gate voltage. Under a positive gate voltage, the HOMO energy level more readily enters the Fermi window. Therefore, charge transport is more significantly modulated by positive gate voltage, which aligns with the FET characteristics of the device. Note that this observation differs from the typical behavior of single-molecule FETs, where a positive gate voltage usually results in downward shift of Frontier molecular orbitals. We attribute this discrepancy to the influence of electric fields, generated by gate voltages of varying directions and magnitudes, on the molecular electronic structure. Specifically, changes in the molecular electrostatic potential (ESP), dipole moment, and dihedral angle between the central SBF unit and the phenyl groups occur under different gate voltages, which are discussed in greater detail in Figures S26–S28.

**NDC Effect and Theoretical Explanation.** Charge transport measurements were conducted on single-molecule devices connected with 2,2-SBF-NH<sub>2</sub> at various temperatures (Figures 4a,b and S23–S24). Figure 4c shows  $I$ – $V$  curves of the device at temperatures of 2, 20, 80, 140, and 200 K, with each curve representing the average of five measurements. Notably, the  $dI/dV$  plots in Figure 4d exhibit an intriguing feature of NDC, characterized by a decrease in the blockade region and a gradual disappearance of the NDC effect as the temperature increases. The presence of NDC and Coulomb blockade features was also observed in  $I$ – $V$  curves of other devices (Figure S25), where variations in the size of the blockade region as well as the value and location of current peaks and valleys may arise due to inherent differences between individual devices.

To elucidate the charge transport characteristics of the molecular junction centered on the SBF, quantum transport

calculations were performed. The theoretical  $I$ - $V$  curve (Figure 4e) of 2,2-SBF-NH<sub>2</sub> molecular junctions further validates this effect, revealing a pronounced NDC phenomenon at low bias voltages. Furthermore, the transmission spectrum of 2,2-SBF-NH<sub>2</sub> exhibits a distinct antiresonance dip (Figure 4f), in contrast to the transmission spectrum of 2,7-SBF-NH<sub>2</sub>, indicating the presence of DQI effect. In Figure 4g, in comparison with the transmission spectrum at a zero bias, the spectra at 0.06 and 0.18 V do not exhibit antiresonance features. The transmission coefficient of the resonance peak at 0.06 V is several orders of magnitude higher than those at other bias voltages. Conversely, at 0.18 V, the transmission coefficient of the resonance peak drops to approximately  $10^{-5}$ . Consequently, in Figure 4e, the current peak and valley appear at bias voltages of 0.06 and 0.18 V, respectively.

Building upon the research conducted previously,<sup>28</sup> it has been demonstrated that Spiro-conjugated structures can engender DQI within the resonant transport region, leading to current blockade effects. Under the driving of bias voltage, the symmetry diminishes as the two conjugated moieties undergo a twist away from 90°, and the system undergoes a pseudo-Jahn-Teller distortion, thereby resulting in the alleviation of DQI. At higher bias voltages, strong electron-electron repulsion impedes further transfer of electrons to the molecule, leading to the NDC effect in certain bias regions. To further explore this phenomenon, we calculated the dihedral angle of the central SBF structure as a function of the EEF strength (induced by bias voltages), as illustrated in Figure 4h. At a zero bias, the dihedral angle of 2,2-SBF-NH<sub>2</sub> is approximately 90°. As the bias voltage increases, the dihedral angle gradually augments. In contrast, the dihedral angle of 2,7-SBF-NH<sub>2</sub> remains relatively constant at approximately 90° with varying bias voltages. Combining these results with the insights provided by the literature,<sup>28</sup> we propose that this structural distortion partially alleviates the DQI effect, ultimately leading to the emergence of NDC.

## CONCLUSIONS

In summary, we integrated SBF units with an orthogonal electronic structure into graphene-based single-molecule devices, thereby observing Coulomb blockade and NDC effects, both of which exhibit significant temperature sensitivity. By leveraging the Coulomb blockade effect, we achieved high on/off ratios in the FET performance. In addition, we find that the NDC effect arises from bias-driven structural distortions, partially alleviating the DQI effect. These findings underscore the potential of SBF-based molecular devices in advancing the field of molecular electronics, offering both practical applications and a deeper understanding of the underlying mechanisms governing charge transport at the nanoscale.

The Coulomb blockade effect could be particularly useful in low-power quantum computing and single-electron transistors, where the ability to control electron tunneling at the nanoscale is crucial for efficient data processing. By fine-tuning gate voltages and optimizing device geometry, it is possible to minimize energy loss and improve the switching accuracy. The NDC effect, on the other hand, shows promise for high-speed memory and oscillator circuits, where rapid and sharp changes in current can enable fast data storage and retrieval. Further optimization through temperature control, material selection, and environmental stability can enhance the robustness of

these effects, making them more viable for large-scale applications. We believe that the continuous exploration of these mechanisms will undoubtedly lead to further advancements in molecular electronics and quantum technologies.

## ASSOCIATED CONTENT

### Supporting Information

The Supporting Information is available free of charge at <https://pubs.acs.org/doi/10.1021/jacs.4c10924>.

Materials and methods, synthesis and characterization, fabrication process of single-molecule devices, additional charge transport data, and theoretical calculations (PDF)

## AUTHOR INFORMATION

### Corresponding Authors

Hao-Li Zhang – State Key Laboratory of Applied Organic Chemistry (SKLAOC), Key Laboratory of Special Function Materials and Structure Design (MOE), College of Chemistry and Chemical Engineering, Lanzhou University, Lanzhou 730000, P. R. China; [orcid.org/0000-0002-6322-5202](https://orcid.org/0000-0002-6322-5202); Email: [haoli.zhang@lzu.edu.cn](mailto:haoli.zhang@lzu.edu.cn)

Xuefeng Guo – Beijing National Laboratory for Molecular Sciences, National Biomedical Imaging Center, College of Chemistry and Molecular Engineering, Peking University, Beijing 100871, P. R. China; Center of Single-Molecule Sciences, Institute of Modern Optics, Frontiers Science Center for New Organic Matter, Tianjin Key Laboratory of Micro-scale Optical Information Science and Technology, College of Electronic Information and Optical Engineering, Nankai University, Tianjin 300350, P. R. China; [orcid.org/0000-0001-5723-8528](https://orcid.org/0000-0001-5723-8528); Email: [guoxf@pku.edu.cn](mailto:guoxf@pku.edu.cn)

### Authors

Caiyao Yang – Beijing National Laboratory for Molecular Sciences, National Biomedical Imaging Center, College of Chemistry and Molecular Engineering, Peking University, Beijing 100871, P. R. China; School of Materials Science and Engineering, Peking University, Beijing 100871, P. R. China

Jiawen Cao – Beijing National Laboratory for Molecular Sciences, National Biomedical Imaging Center, College of Chemistry and Molecular Engineering, Peking University, Beijing 100871, P. R. China

Jin-Liang Lin – State Key Laboratory of Applied Organic Chemistry (SKLAOC), Key Laboratory of Special Function Materials and Structure Design (MOE), College of Chemistry and Chemical Engineering, Lanzhou University, Lanzhou 730000, P. R. China

Hao Wu – Beijing National Laboratory for Molecular Sciences, National Biomedical Imaging Center, College of Chemistry and Molecular Engineering, Peking University, Beijing 100871, P. R. China

Complete contact information is available at: <https://pubs.acs.org/10.1021/jacs.4c10924>

### Author Contributions

<sup>†</sup>C.Y., J.C., and J.-L.L. contributed equally to this work.

### Notes

The authors declare no competing financial interest.

## ACKNOWLEDGMENTS

The authors acknowledge primary financial support from the National Key R&D Program of China (2022YFE0128700, 2021YFA1200101, and 2023YFF1205803) and the National Natural Science Foundation of China (22150013, 21727806, 21933001, 92256202, U22A20399, and 22221001), “Frontiers Science Center for New Organic Matter” at Nankai University (63181206), the Natural Science Foundation of Beijing (2222009), Beijing National Laboratory for Molecular Sciences (BNLMS-CXXM-202407), and the 111 project 2.0 (BP1221004). The authors also thank Supercomputing Center of Lanzhou University for providing the computing time.

## REFERENCES

- (1) Simmons, H. E.; Fukunaga, T. Spiroconjugation. *J. Am. Chem. Soc.* **1967**, *89*, 5208–5215.
- (2) Hoffmann, R.; Imamura, A.; Zeiss, G. D. Spirarenes. *J. Am. Chem. Soc.* **1967**, *89*, 5215–5220.
- (3) Saragi, T. P. I.; Spehr, T.; Siebert, A.; Fuhrmann-Lieker, T.; Salbeck, J. Spiro compounds for organic optoelectronics. *Chem. Rev.* **2007**, *107*, 1011–1065.
- (4) Chen, H.; Zeng, J.; Huang, R.; Wang, J.; He, J.; Liu, H.; Yang, D.; Ma, D.; Zhao, Z.; Tang, B. Z. An efficient aggregation-enhanced delayed fluorescence luminogen created with spiro donors and carbonyl acceptor for applications as an emitter and sensitizer in high-performance organic light-emitting diodes. *Aggregate* **2023**, *4*, No. e244.
- (5) Rombach, F. M.; Haque, S. A.; Macdonald, T. J. Lessons learned from spiro-OMeTAD and PTAA in perovskite solar cells. *Energy Environ. Sci.* **2021**, *14*, 5161–5190.
- (6) Zhang, T.; Wang, F.; Kim, H.-B.; Choi, I.-W.; Wang, C.; Cho, E.; Konefal, R.; Puttison, Y.; Terado, K.; Kobera, L.; Chen, M.; Yang, M.; Bai, S.; Yang, B.; Suo, J.; Yang, S.-C.; Liu, X.; Fu, F.; Yoshida, H.; Chen, W. M.; Brus, J.; Coropceanu, V.; Hagfeldt, A.; Brédas, J. L.; Fahlman, M.; Kim, D. S.; Hu, Z.; Gao, F. Ion-modulated radical doping of spiro-OMeTAD for more efficient and stable perovskite solar cells. *Science* **2022**, *377*, 495–501.
- (7) Jeong, M.; Choi, I. W.; Yim, K.; Jeong, S.; Kim, M.; Choi, S. J.; Cho, Y.; An, J.-H.; Kim, H.-B.; Jo, Y.; Kang, S.-H.; Bae, J.-H.; Lee, C.-W.; Kim, D. S.; Yang, C. Large-area perovskite solar cells employing spiro-Naph hole transport material. *Nat. Photonics* **2022**, *16*, 119–125.
- (8) Yu, X.; Chen, L.; Li, C.; Gao, C.; Xue, X.; Zhang, X.; Zhang, G.; Zhang, D. Intrinsically stretchable polymer semiconductors with good ductility and high charge mobility through reducing the central symmetry of the conjugated backbone units. *Adv. Mater.* **2023**, *35*, 2209896.
- (9) Zhang, K.; Kotadiya, N. B.; Wang, X.-Y.; Wetzelaer, G.-J. A. H.; Marszalek, T.; Pisula, W.; Blom, P. W. M. Interlayers for improved hole injection in organic field-effect transistors. *Adv. Electron. Mater.* **2020**, *6*, 1901352.
- (10) Gerhard, L.; Edelmann, K.; Homberg, J.; Valásek, M.; Bahoosh, S. G.; Lukas, M.; Pauly, F.; Mayor, M.; Wulfhekel, W. An electrically actuated molecular toggle switch. *Nat. Commun.* **2017**, *8*, 14672.
- (11) Karimi, M. A.; Bahoosh, S. G.; Valásek, M.; Bürkle, M.; Mayor, M.; Pauly, F.; Scheer, E. Identification of the current path for a conductive molecular wire on a tripod platform. *Nanoscale* **2016**, *8*, 10582–10590.
- (12) Valásek, M.; Edelmann, K.; Gerhard, L.; Fuhr, O.; Lukas, M.; Mayor, M. Synthesis of molecular tripods based on a rigid 9,9'-spirobifluorene scaffold. *J. Org. Chem.* **2014**, *79*, 7342–7357.
- (13) Greenwald, J. E.; Cameron, J.; Findlay, N. J.; Fu, T.; Gunasekaran, S.; Skabara, P. J.; Venkataraman, L. Highly nonlinear transport across single-molecule junctions via destructive quantum interference. *Nat. Nanotechnol.* **2021**, *16*, 313–317.
- (14) Xin, N.; Li, X.; Jia, C.; Gong, Y.; Li, M.; Wang, S.; Zhang, G.; Yang, J.; Guo, X. Tuning charge transport in aromatic-ring single-molecule junctions via ionic-liquid gating. *Angew. Chem., Int. Ed.* **2018**, *57*, 14026–14031.
- (15) Perrin, M. L.; Frisenda, R.; Koole, M.; Seldenthuis, J. S.; Gil, J. A. C.; Valkenier, H.; Hummelen, J. C.; Renaud, N.; Grozema, F. C.; Thijssen, J. M.; Dulić, D.; van der Zant, H. S. J. Large negative differential conductance in single-molecule break junctions. *Nat. Nanotechnol.* **2014**, *9*, 830–834.
- (16) Andrews, D. Q.; Solomon, G. C.; Van Duynne, R. P.; Ratner, M. A. Single molecule electronics: increasing dynamic range and switching speed using cross-conjugated species. *J. Am. Chem. Soc.* **2008**, *130*, 17309–17319.
- (17) Li, P.; Hou, S.; Alharbi, B.; Wu, Q.; Chen, Y.; Zhou, L.; Gao, T.; Li, R.; Yang, L.; Chang, X.; Dong, G.; Liu, X.; Decurtins, S.; Liu, S.-X.; Hong, W.; Lambert, C. J.; Jia, C.; Guo, X. Quantum interference-controlled conductance enhancement in stacked graphene-like dimers. *J. Am. Chem. Soc.* **2022**, *144*, 15689–15697.
- (18) Bai, J.; Daaoub, A.; Sangtarash, S.; Li, X.; Tang, Y.; Zou, Q.; Sadeghi, H.; Liu, S.; Huang, X.; Tan, Z.; Liu, J.; Yang, Y.; Shi, J.; Meszaros, G.; Chen, W.; Lambert, C. J.; Hong, W. Anti-resonance features of destructive quantum interference in single-molecule thiophene junctions achieved by electrochemical gating. *Nat. Mater.* **2019**, *18*, 364–369.
- (19) Gehring, P.; Thijssen, J. M.; van der Zant, H. S. J. Single-molecule quantum-transport phenomena in break junctions. *Nat. Rev. Phys.* **2019**, *1*, 381–396.
- (20) Schmidt, H. C.; Larsen, C. B.; Wenger, O. S. Electron transfer around a molecular corner. *Angew. Chem., Int. Ed.* **2018**, *57*, 6696–6700.
- (21) Aviram, A. Molecules for memory, logic, and amplification. *J. Am. Chem. Soc.* **1988**, *110*, 5687–5692.
- (22) Xiang, D.; Wang, X.; Jia, C.; Lee, T.; Guo, X. Molecular-scale electronics: from concept to function. *Chem. Rev.* **2016**, *116*, 4318–4440.
- (23) Xin, N.; Guan, J.; Zhou, C.; Chen, X.; Gu, C.; Li, Y.; Ratner, M. A.; Nitzan, A.; Stoddart, J. F.; Guo, X. Concepts in the design and engineering of single-molecule electronic devices. *Nat. Rev. Phys.* **2019**, *1*, 211–230.
- (24) Sun, L.; Diaz-Fernandez, Y. A.; Gschneidner, T. A.; Westerlund, F.; Lara-Avila, S.; Moth-Poulsen, K. Single-molecule electronics: from chemical design to functional devices. *Chem. Soc. Rev.* **2014**, *43*, 7378–7411.
- (25) Yang, C.; Yang, C.; Guo, Y.; Feng, J.; Guo, X. Graphene–molecule–graphene single-molecule junctions to detect electronic reactions at the molecular scale. *Nat. Protoc.* **2023**, *18*, 1958–1978.
- (26) Cao, Y.; Dong, S.; Liu, S.; He, L.; Gan, L.; Yu, X.; Steigerwald, M. L.; Wu, X.; Liu, Z.; Guo, X. Building high-throughput molecular junctions using indented graphene point contacts. *Angew. Chem., Int. Ed.* **2012**, *51*, 12228–12232.
- (27) Yang, C.; Shen, P.; Ou, Q.; Peng, Q.; Zhou, S.; Li, J.; Liu, Z.; Zhao, Z.; Qin, A.; Shuai, Z.; Tang, B. Z.; Guo, X. Complete deciphering of the dynamic stereostructures of a single aggregation-induced emission molecule. *Matter* **2022**, *5*, 1224–1234.
- (28) Sowa, J. K.; Mol, J. A.; Briggs, G. A. D.; Gauger, E. M. Spiro-conjugated molecular junctions: between Jahn-Teller distortion and destructive quantum interference. *J. Phys. Chem. Lett.* **2018**, *9*, 1859–1865.
- (29) Park, J.; Pasupathy, A. N.; Goldsmith, J. I.; Chang, C.; Yaish, Y.; Petta, J. R.; Rinkoski, M.; Sethna, J. P.; Abruna, H. D.; McEuen, P. L.; Ralph, D. C. Coulomb blockade and the Kondo effect in single-atom transistors. *Nature* **2002**, *417*, 722–725.
- (30) Chen, Z.; Grace, I. M.; Woltering, S. L.; Chen, L.; Gee, A.; Baugh, J.; Briggs, G. A. D.; Bogani, L.; Mol, J. A.; Lambert, C. J.; Anderson, H. L.; Thomas, J. O. Quantum interference enhances the performance of single-molecule transistors. *Nat. Nanotechnol.* **2024**, *19*, 986–992.
- (31) Yang, C.; Chen, Z.; Yu, C.; Cao, J.; Ke, G.; Zhu, W.; Liang, W.; Huang, J.; Cai, W.; Saha, C.; Sabuj, M. A.; Rai, N.; Li, X.; Yang, J.; Li, Y.; Huang, F.; Guo, X. Regulation of quantum spin conversions in a single molecular radical. *Nat. Nanotechnol.* **2024**, *19*, 978–985.

(32) Black, C. T.; Murray, C. B.; Sandstrom, R. L.; Sun, S. Spin-dependent tunneling in self-assembled cobalt-nanocrystal superlattices. *Science* **2000**, *290*, 1131–1134.

(33) Fan, H.; Yang, K.; Boye, D. M.; Sigmon, T.; Malloy, K. J.; Xu, H.; López, G. P.; Brinker, C. J. Self-assembly of ordered, robust, three-dimensional gold nanocrystal/silica arrays. *Science* **2004**, *304*, 567–571.

(34) Selzer, Y.; Cabassi, M. A.; Mayer, T. S.; Allara, D. L. Thermally activated conduction in molecular junctions. *J. Am. Chem. Soc.* **2004**, *126*, 4052–4053.

(35) Zhu, X.; Wang, B.; Xiong, W.; Zhou, S.; Qu, K.; Lü, J.; Chen, H.; Jia, C.; Guo, X. Vibration-assisted charge transport through positively charged dimer junctions. *Angew. Chem., Int. Ed.* **2022**, *61*, No. e202210939.

(36) Yuan, L.; Wang, L.; Garrigues, A. R.; Jiang, L.; Annadata, H. V.; Anguera Antonana, M.; Barco, E.; Nijhuis, C. A. Transition from direct to inverted charge transport Marcus regions in molecular junctions via molecular orbital gating. *Nat. Nanotechnol.* **2018**, *13*, 322–329.

(37) Chen, X.; Jeon, Y. M.; Jang, J. W.; Qin, L.; Huo, F.; Wei, W.; Mirkin, C. A. On-wire lithography-generated molecule-based transport junctions: a new testbed for molecular electronics. *J. Am. Chem. Soc.* **2008**, *130*, 8166–8168.

(38) Sarker, B. K.; Khondaker, S. I. Thermionic emission and tunneling at carbon nanotube–organic semiconductor interface. *ACS Nano* **2012**, *6*, 4993–4999.

(39) Kim, J. Y.; Lee, S.; Yoo, K. H.; Jang, D. Coulomb blockade effect and negative differential resistance in the electronic transport of bacteriorhodopsin. *Appl. Phys. Lett.* **2009**, *94*, 153301.

(40) Courtin, J.; Tricot, S.; Delhay, G.; Turban, P.; Lépine, B.; Le Breton, J. C.; Schieffer, P. Origin of weak Fermi level pinning at the graphene/silicon interface. *Phys. Rev. B* **2020**, *102*, 245301.

(41) Song, H.; Kim, Y.; Jang, Y. H.; Jeong, H.; Reed, M. A.; Lee, T. Observation of molecular orbital gating. *Nature* **2009**, *462*, 1039–1043.

(42) Kim, W. Y.; Kim, K. S. Tuning Molecular Orbitals in molecular electronics and spintronics. *Acc. Chem. Res.* **2010**, *43*, 111–120.